1 Tools of the Trade: Electrical and Optical Recording and Perturbation of Neuronal Activity

1.1 Scale of Thermal Fluctuations

Neurons use voltage levels of order $k_B T/e$ and voltage dependent conductance, to shift between the two levels. We now re-examine this viewpoint in terms of synaptic transmission and noise immunity on the one hand, and the trade-off between noise and the speed of a networks response on the other hand.

The fundamental voltage scale is the thermal scale, or

$$\frac{k_B T}{e} \approx 25 \ mV. \tag{1.1}$$

We now consider the smallest scale, that of thermal noise, in driving intrinsic fluctuations in the membrane voltage. Ion flow across the membrane is defined by a net conductance, G, across the cell. One way to derive the equation for the thermal noise is to use the equipartition theorem to equate the fluctuating energy in the membrane to the thermal energy, i.e.,

$$\frac{1}{2}C\delta V^2 = \frac{1}{2}k_B T \tag{1.2}$$

This leads to a fluctuation in the potential (Figure 1) of size

$$\delta V = \sqrt{\frac{k_B T}{C}}. \tag{1.3}$$

A different derivation is given in **Box 1**. This noise has the same spectral power density at all frequencies. This is different that other sources of noise, like $1/f$ noise, that has origins in processes occurring of a variety of energy scales (Figure 2).

The capacitance is measure of geometry and electric susceptibility ϵ. It is given by $C = \epsilon_m \ (\text{area/thickness})$, so that for a thin dielectric sphere of thickness L and radius a, $C = \epsilon_m \frac{4\pi a^2}{L}$. Thus

$$\delta V = \sqrt{\left(\frac{k_B T}{e}\right)\left(\frac{L}{\epsilon_m}\right)\frac{e}{4\pi a^2}} \tag{1.4}$$

$$= \frac{1}{2a}\sqrt{\left(\frac{k_B T}{e}\right)\left(\frac{e}{c_m}\right)\frac{1}{\pi}}.$$

For most all cells, the ratio $\frac{\epsilon_m}{L}$ is

$$c_m \equiv \frac{\epsilon_m}{L} \tag{1.5}$$

$$\approx 0.9 x 10^{-14} \frac{F}{\mu m^2}$$

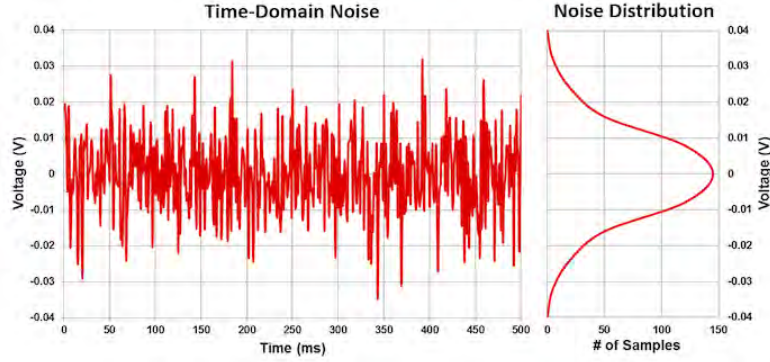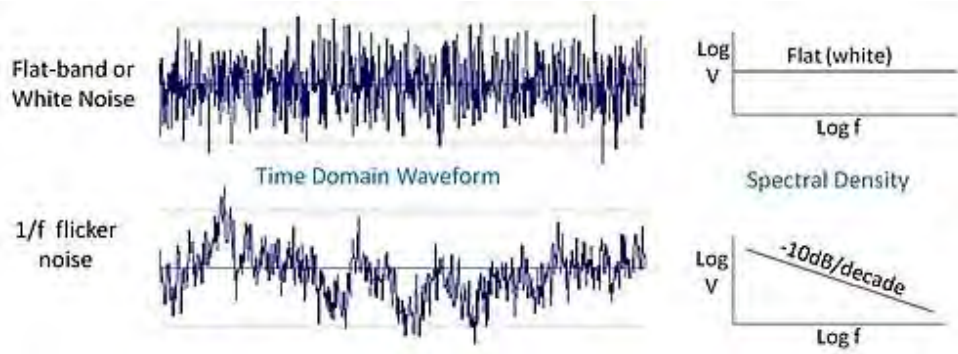Figure 1: Thermal noise and the Gaussian amplitude distribution.

Figure 2: Thermal noise with a white - or flat - spectrum and flicker or Brownian noise - with a f^{-1} amplitude or f^{-2} spectrum.

and

$$\frac{e}{c_m} = 1.8 \times 10^{-2} \frac{mV}{\mu m^2} \tag{1.6}$$

so that

$$\delta V \approx \frac{190 \mu V}{a \ (\text{in } \mu m)}. \tag{1.7}$$

For a cell of radius $a = 10 \mu m$,

$$\delta V \approx 20 \mu V. \tag{1.8}$$

Thus:

- The membrane noise level for cell somata is much less, by three orders of magnitude, then the thermal voltage $k_B T / e$.

- The membrane noise level for is less, by one order of magnitude, than the typical minimal synaptic input.

2

1.2   Measurement fundamentals

1.2.1   Electrical

Lossy devices like electrodes, and the membrane of cells as discussed above, have a noise associated with the random movement of charge carriers. This can be expressed in a general way in terms of the fluctuation-dissipation theorem that relates the loss in energy in a device to the level of fluctuation in the transport of a quantity, such a charge. Thus for the case of electrical circuits, an initial current through a closed loop that contains a resistor will rapidly tend toward zero. This occurs because the resistance dissipates electrical energy, turning it into heat (Joule heating). However, there is a random fluctuating current flow through the resistor that is caused by the thermal fluctuations of the electrons in the resistor. This is called Johnson noise. It has zero mean and a variance of δI_J^2 given by

$$\delta I_J^2 = \frac{4k_B T \Delta \nu}{R}. \tag{1.9}$$

By the way, this for a single-channel patch electrode, this current must be less than the current in a channel, so R must be big enough!

A complementary view to look at noise is the voltage in an open circuit across the resistor. Here the variance of the voltage noise is

$$\delta V_J^2 = 4k_B T R \Delta \nu. \tag{1.10}$$

. For a scenario in which the noise is 10-times less than that of the $20 \mu V$ intracellular membrane noise and the bandwidth matches that of the rise time of the action potential, requiring $\Delta \nu = 10$ kHz, we find $R \simeq 200$ MΩ. This reflects the reality for intracellular electrodes. A patch electrode can have considerable less resistance, maybe $R \approx 200$ kΩ.

The second issue is that the voltage probe should not draw any current, which is to say that the resistance should be large. This means that the amplifier used with the electrode must have an input resistance large compared to the electrode resistance, on the the range of tens of GOhms; this is reasonable with FET-input amplifiers. In general, the impedance of the probe must be large compared to that of the source - or system under study - to avoid perturbing the source.

1.2.2   Optical

Measurements of light, such as that emitted from a fluorescent source, are fundamentally limited by the Poisson arrival statistics of photons. Achieving this limit requires that all systematic noise sources, such as an excitation light, are minimized. Shot noise is expressed as a current δI, i.e.,

$$\delta I = \sqrt{2eI\Delta \nu} \tag{1.11}$$

where e is the electronic charge and I is the total current. Typically, the signal that is measured corresponds to a change in the intensity of light, of a change in I denoted ΔI. Then the signal-to-noise ratio (SNR) is

$$SNR \;=\; \frac{\Delta I}{\delta I} \tag{1.12}$$

3

$$= \frac{\Delta I}{I} \sqrt{\frac{I}{2e\Delta\nu}}.$$

As a practical matter, optical detectors are current sources. They ideally drive a load with zero impedance so that a voltage difference in not developed across the device. This is readily achieved using an op-amp configured as a current-to-voltage circuit. The input impedance is the feedback resistance, R, divided by the open-loop-gain, which is easily 10^6. Thus a nanoAmp of current is converted to 1 milliVolt using R = 1 MOhm with an input resistance of only 1 Ohm. A second amplifier can provide additional gain.

Equation 1.13 is an important formula. It states that the SNR varies as the fraction change of the indicator - say a popular calcium indicator like GCaMP - times the square-root of the intensity of the light. We can turn this into numbers of photons, n,

$$SNR = \frac{\Delta n}{n} \sqrt{n} \tag{1.13}$$

which clearly states that smaller signals require more photons or more measurements to achieve a reliable estimate.

As a second practical matter, optical imaging is limited by the absorption of light by water to a region of about 250 nm to 1.7 μm (Figure 3). Further, the absorption of light by both oxyhemoglobin and deoxyhemoglobin suggests the use of light that is longer than 630 nm in imaging with vascularized animals, both for the excitation and the emission wavelengths (Figure 4).

Figure 3: The absorprption spectrum of water from the far ultraviolet to microwaves
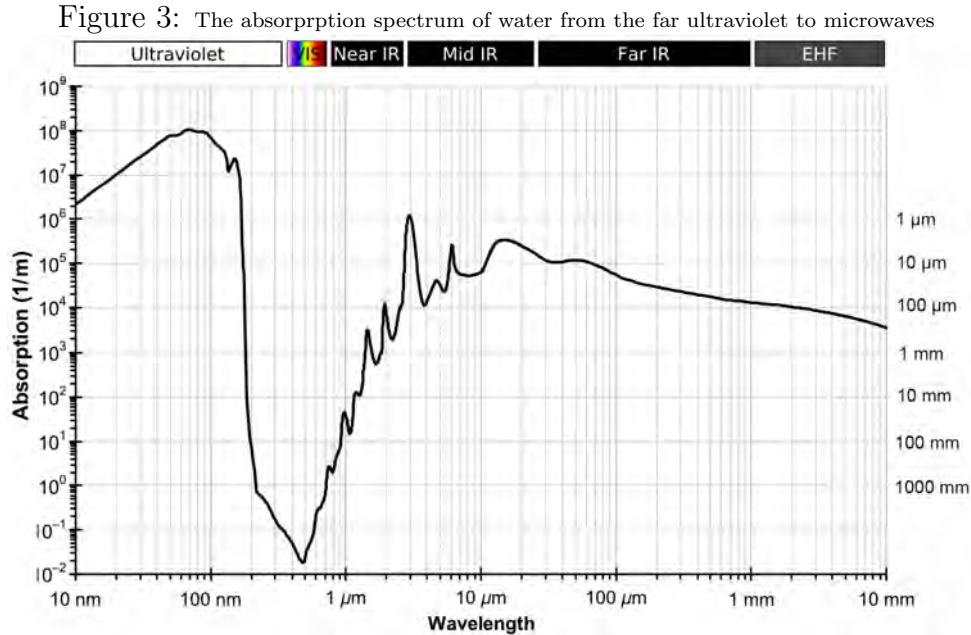
1.2.3 Information and SNR

We saw (Eq 1.13) that the signal-to-noise increases as we make more and more measurements. So when do we stop? A principled way to think about this is in terms of the

Figure 4: The absorprption spectrum of heme in water from violet light to the near infrared, with annotations for windows used in two-photon imaging ca 2020
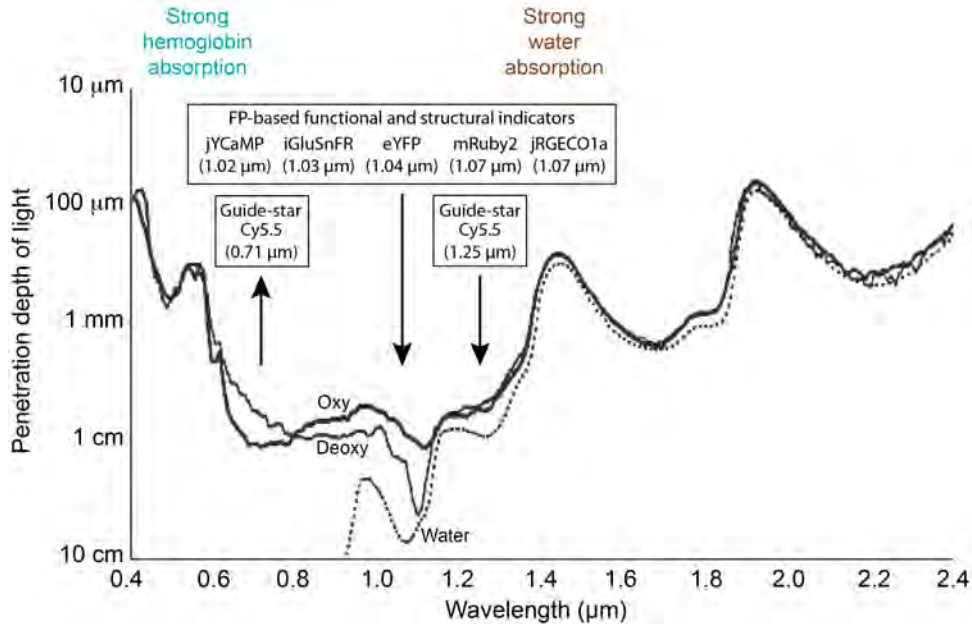
transfer of information about the system from repeated measurements. Here the noise may also include terms from the biological system and various technological sources in addition to fundamentals such as shot noise. Nonetheless, for specific models of the noise, we can calculate the information gained about a system from continued measurements. For quantification in terms of mutual information, denoted I_M, and noise assumed to follow Gaussian statistics, which is reasonable for large numbers of measurements, we note the classic result (**Box 2**)

$$I_M = \frac{1}{2} \log \left[1 + (SNR)^2 \right] \tag{1.14}$$

where the square occurs because are need to convert to power, e.g., (voltage)^2. This states that the mutual informal rises linearly when the SNR is small, i.e., $I_M \simeq SNR/2$ (recall $\ln(1+x) \approx x$ for $x << 1$), and then rises only slowly for when the SNR becomes large, i.e, $I_M \simeq log(SNR)$. So, if experimental time is limited and many sites need to be observed, one should only measure until the SNR reaches say 10-ish, then move on!

1.3   Modern twists on electrodes

Classical intracellular recording makes use of glass cylindrical electrodes that provide an intracellular connection to a cell. The modern twist is intracellular recording from a cortical or hippocampal neurons in a mouse that is running on a maze (Figure 5). This shows, for example, that neurons can have so much excitatory drive at the center of their receptive field that the cell is essentially shunted (Figure 6); this phenomena would be missed by extracellular electrodes.

Classical extracellular recording makes use of metal electrodes that record the flow of

current outside of a cell and provide a means to infer spikes in a neighboring cell. The modern twist is extracellular recording from hundreds of sites at once (Figure 7). The site density is high enough to match waveforms across upwards of ten electrodes and time, which makes spike sorting a template matching problem in space-time (Figure 8).

1.4 Holistic measures of spiking and behavior

The modern twist of extracellular recording from hundreds of sites at once (Figure 7) has been employed with freely moving animals and recording of animal motion in a naturalistic spatial environment. This involved coordinated measures of motion (accelerometers), images from multiple cameras, and optical photometry with electrode recording. Further, this is accomplished in a manner that allows high-bandwidth data movement without impending the movement of the animal through torque in the tether (Figure 9). Feedback from spike behavior to electrical and optical perturbation signals is accomplished in ¡ 0.5 s (Figure 10).

1.5 Genetically expressed optical-based indicators of intracellular Ca^{2+}.

In a program started by the late Roger Tsien, these molecules (Figure 1.12) are expressed in vivo in specific cell types and initiate an increase in fluorescence in response to the Ca^{2+} influx that follows an action potential (Figure 12). The latest version from Looger in GCaMP8 (Figure 13),

1.6 In vivo recording of neuronal structure and function with two-photon laser scanning microscopy

Denk's technique of two-photon laser scanning microscopy, properly pushed to the limit with corrections for the wavefront distortion through tissue (Figure 14), allows changes in intracellular Ca^{2+} to be measured in neuronal soma down to spines in nearly all layers of cortex (Figure 15). Note that the region of observation, the point spread function, is elongated in "z" (Figure 16).

1.7 In vivo recording of calcium signaling with two-photon laser scanning microscopy

In vivo Ca^{2+} signals may be recorded after a single spike, and from many sites (Figure 17). Still the interpretation in terms of numbers of spikes is imperfect and thus curation is suggested in quantitative interpretation of signals (Figures 1.12, 19, and 20).

1.8 The technological front of two-photon laser scanning microscopy

In vivo Ca^{2+} signals may be recorded deep in the brain using adaptive optics to correct for the wavefront of light as it scatters going deeper into the brain (Figure ??). Another

push is the use of miniature, recently 2-1/2 g, head mounted two-photon microscopes (Figure 21). Together with a prism, these were used to measure for Grid cells in the medial entorhinal cortex (Figure 22).

1.9 In vivo recording of neuronal structure and function with light sheet scanning microscopy

A linear method of optical sectioning, properly pushed to the limit with corrections for the wavefront distortion through tissue (Figures 23 and 24), allows structure of changes in intracellular Ca^{2+} to be measured in tissue (Figure 25). Sectioning occurs through perpendicular excitation and recording beams, so that lateral resolution sets the z-resolution. This technique can be fast and efficient, albeit the illumination is sometimes used through thick tissue and distorted by index changes

1.10 In vivo recording of activity in the locomoting animal

The use of virtual reality in combination with two-photon microscopy permits behavior and circuit dynamics to be concurrently measured (Figures 26 and 27). Simplified set-ups work very well ((Figures 28).

1.11 Genetically expressed optical-based drivers of spiking

Optical activation of certain microbial opsin expressed in the membrane of neurons (Figure 29), most famously channelrhodopsin (Figure 30), can be used to photo-excite, or photo-inhibit, neurons.

1.12 All optical schemes for feedback control of spiking

The use of two-photon imaging and concurrent two-photon photoactivation, plus virtual reality, permits behavior and circuit dynamics to be concurrently measured and perturbed solely with light and light-activated molecules (Figures 31, 32, 33, 34, and 35).

Box 1. Self-consistency. Note that a resistor also has a nonzero capacitance between the leads, denoted C. The parallel combination of R and C will lead to a low pass filter with time constant RC. Thus the bandwidth will be limited to a maximum of $\Delta\nu \approx 1/RC$. A more precise estimate can be found by equating the decrement in power for a RC low-pass filter with $\Delta\nu$, *i.e.*,

$$\Delta\nu = \frac{1}{2\pi} \int_0^\infty d\omega \; \frac{1}{1 + (\omega/RC)^2} = \frac{1}{4RC}. \tag{1.15}$$

Thus the variance of the voltage noise can also be expressed as

$$\delta V_J^2 = 4k_B T R \frac{1}{4RC} = \frac{k_B T}{C} \tag{1.16}$$

which is the equipartition result we started with above.

Box 2. Mutual Information and Signal-to-Noise We start with the definition of conditional probability. Let $P(r|s)$ be fined as the probability of a response r given a stimulus s. Then the associated Shannon information, denoted H, or equivalently the entropy of the response, is

$$H(r,s) = -\int dr\ P(r|s)\log P(r|s) \tag{1.17}$$

The question is if this is larger than a random response. This leads to the definition of the noise entropy, denoted H_{noise}, as an average entropy over all stimuli. Thus

$$
\begin{aligned}
H_{noise}(r,s) &= \int ds\ P(s)H(r,s) \\
&= -\int\int ds\ dr\ P(s)P(r|s)\log P(r|s)
\end{aligned} \tag{1.18}
$$

The difference between the entropy of the response, denoted $H_s(r)$ where

$$H(r) = -\int dr\ P(r)\log P(r) \tag{1.19}$$

and $H_{noise}(r,s)$ is the a measure of what can be gleamed about the stimulus from the response. This is known as the mutual information, denoted I_m, where

$$
\begin{aligned}
I_M &= H(r) - H_{noise}(r,s) \\
&= -\int dr\ P(r)\log P(r) + \int\int ds\ dr\ P(s)P(r|s)\log P(r|s)
\end{aligned} \tag{1.20}
$$

To simply this, we know that we can express $P(r)$ and a sum the conditional probability $P(r|s)$ summed over all stimuli, or

$$P(r) = -\int dr\ P(r|s)P(s) \tag{1.21}$$

Then

$$
\begin{aligned}
I_M &= -\int\int dr\ ds\ P(r|s)P(s)\log P(r) + \int\int ds\ dr\ P(s)P(r|s)\log P(r|s) \tag{1.22} \\
&= \int\int ds\ dr\ P(r|s)P(s)\log\frac{P(r|s)}{P(r)}
\end{aligned}
$$

We can go one more step and express this in terms of the joint probability $P(r,s)$, i.e. the probability of r and s, where

$$
\begin{aligned}
P(r,s) &= P(r|s)P(s) \tag{1.23} \\
&\text{or} \\
P(r,s) &= P(s|r)P(r).
\end{aligned}
$$

For completeness, note that we have just written Bayes' Theorem, or

$$P(s|r) = P(s)\frac{P(r|s)}{P(r)} \tag{1.24}$$

8

where $P(s|r)$ is denoted the posterior probability, $P(r)$ is denoted the prior probability, $P(r|s)$ is denoted the likelihood and $P(r)$ is denoted the marginal probability.

We now write

$$I_M = \int \int ds \, dr \, P(r,s) \log \frac{P(r,s)}{P(r) \, P(s)} \tag{1.25}$$

which is zero if the stimulus and the response are uncorrelated, i.e., if $P(r,s) = P(r) \, P(s)$. Note the alternate expressions (useful below)

$$I_M = \int \int ds \, dr \, P(r,s) \log \frac{P(r|s)}{P(r)} \tag{1.26}$$

or

$$I_M = \int \int ds \, dr \, P(r,s) \log \frac{P(s|r)}{P(r)}.$$

Let's calculate the mutual information when the stimulus and response both can be modeled as Gaussian random variables.

- Linear response gives

$$r = Gs + \eta \tag{1.27}$$

 where G is the gain of the transduce and η is the additive noise of the transducer, with variance σ^2. This is the output noise of the system; the noise referred to the input is σ^2/G^2.

- Let the stimulus s have an average of $< s >= 0$ and a variance $< s^2 >$. Here $< s^2 >$. is the signal, i.e., the mean-square of changes in the input about the mean.

- Let the response r, or output of the transducer, have an average of $< r >= 0$ and a variance $< r^2 >$. The probability distribution for the response is

-
$$P(r) = \frac{1}{\sqrt{2\pi < r^2 >}} e^{-r^2/2<r^2>} \tag{1.28}$$

Using the notation

$$\langle f(r) \rangle \equiv \int dr \, P(r) f(r) \tag{1.29}$$

The entropy $H(r)$ of this distribution is

$$
\begin{aligned}
H(r) &= -\langle \log P(r) \rangle \tag{1.30}\\
&= -\frac{1}{\ln 2} \Big\langle \frac{1}{2} \ln \left(2\pi < r^2 > \right) + \frac{r^2}{2 < r^2 >} \Big\rangle \\
&= -\frac{1}{\ln 2} \left[\frac{1}{2} \ln \left(2\pi < r^2 > \right) + \frac{< r^2 >}{2 < r^2 >} \right] \\
&= -\frac{1}{2 \ln 2} \left[\ln \left(2\pi < r^2 > \right) + 1 \right]
\end{aligned}
$$

where we used $\log_2 x = (1/\ln 2) \ln x$.

Lets now consider the conditional probability of the response given the stimulus, i.e.,

$$P(r|s) = \frac{1}{\sqrt{2\pi\sigma^2}} e^{-(r-Gs)^2/2\sigma^2} \tag{1.31}$$

where Gs is the mean response. Using the previous notation

$$\langle f(r)\rangle \equiv \int dr \ P(r,s)f(r) \tag{1.32}$$

and the alternate form for I_M (Eq 1.27), we have

$$
\begin{aligned}
I_M \ &= \ \left\langle \log \frac{P(r|s)}{P(r)} \right\rangle \\[2mm]
&= \ \frac{1}{\ln 2}\left[-\frac{-1}{2}\ln\left(2\pi\sigma^2\right) + \frac{1}{2}\ln\left(2\pi <r^2> \right) - \frac{<(r-Gs)^2>}{2\sigma^2} + \frac{<r^2>}{2<r^2>}\right] \\[2mm]
&= \ -\frac{1}{2\ln 2}\left(\ln \frac{<r^2>}{\sigma^2} - \frac{<\sigma^2>}{\sigma^2} + \frac{<r^2>}{<r^2>}\right) \\[2mm]
&= \ -\frac{1}{2\ln 2}\ln \frac{G^2 <s^2> + \sigma^2}{\sigma^2}
\end{aligned}
$$

$$\tag{1.34}$$

where we used $<r^2> = G^2 <s_2> +\sigma^2$, since $<s\,\eta> = 0$ and $<\eta^2> \equiv \sigma^2$. Then

$$I_M = \frac{1}{2}\log\left(1 + \frac{<s^2>}{\sigma^2/G^2}\right) \tag{1.35}$$

Recall that σ^2/G^2 is the noise power referred the input, so this is in the form of the general relation $I_M = (1/2)\log\left[1 + (SNR)^2\right]$ (Eqn. 1.14), where the signal-to-noise ratio is the quotient of the standard deviation of the signal to the standard deviation of the noise at the input.

Figure 5: Head-mount for jerk-free insertion of an electrode into a pyramidal cell. From Lee, Manns, Sakmann and Brecht, 2006
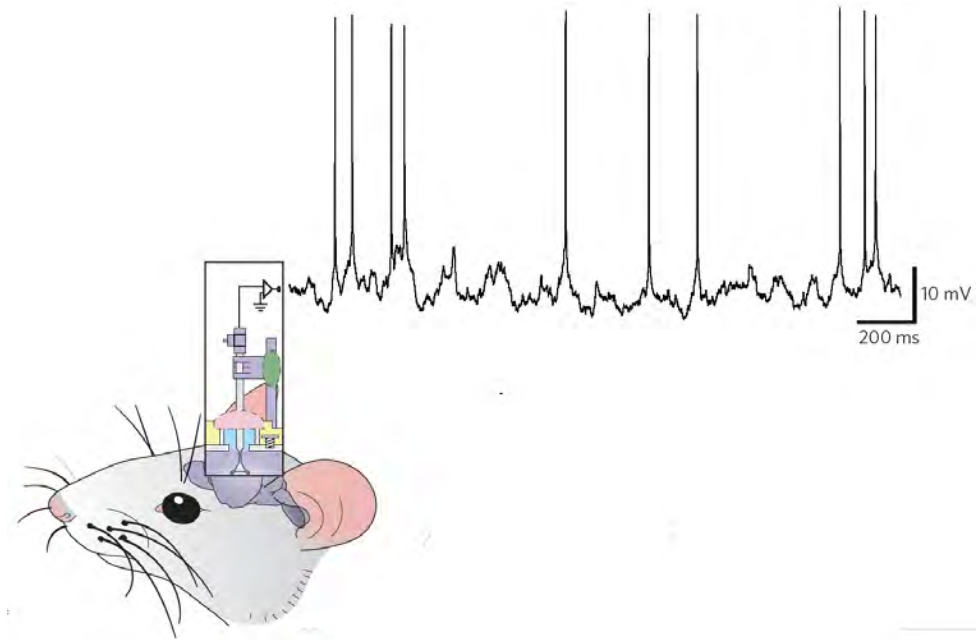
Figure 6: Recording from neurons in CA1 of hippocampus as the mouse passes through its place field; bursts of spikes occurred at regions marked by red dots. From Epsztein, Brecht and Lee, 2011
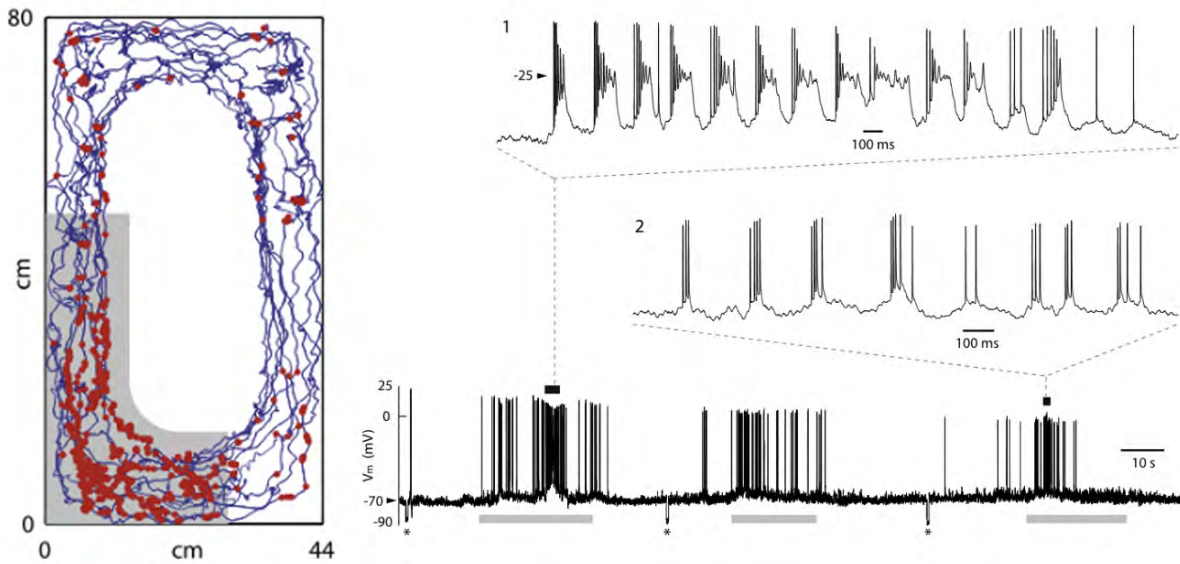
Figure 7: Recording from cortex with Neuropixels. From Jun, Steinmetz, Siegle, Denman, Bauza, Barbarits, Lee, Anastassiou, Andrei, Aydon, Barbic, Blanche, Bonin, Couto, Dutta, Gratiy, Gutnisky, Hausser, Karsh, Ledochowitsch, Lopez, Mitelut, Musa, Okun, Pachitariu, Putzeys, Rich, Rossant, Sun, Svoboda, Carandini, Harris, Koch, O'Keefe and Harris, 2017
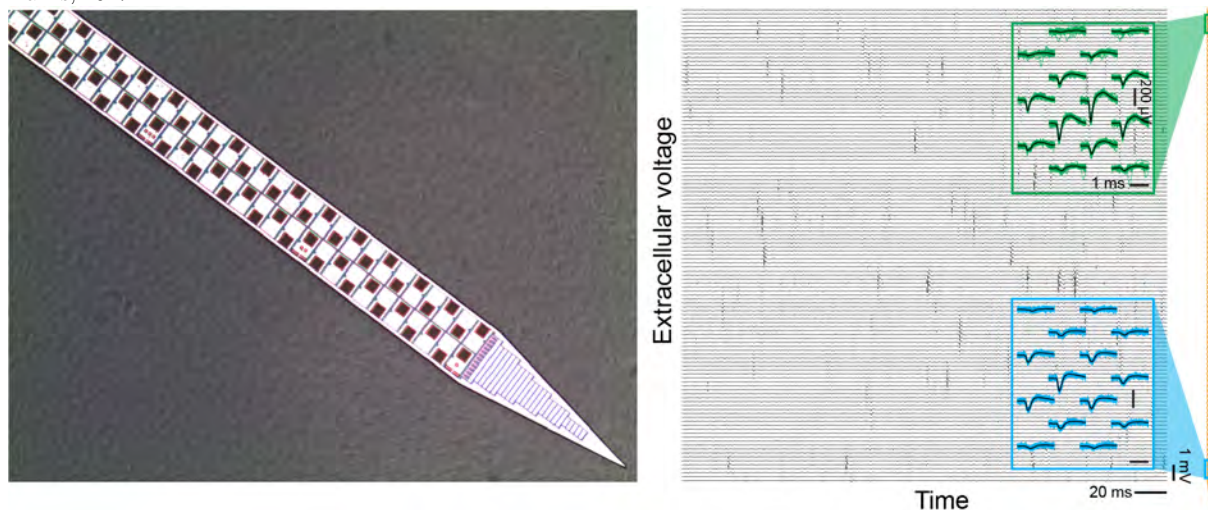
Figure 8: Spike detection and feature extraction with kilosort and neuropixels probes. a, Short segment of preprocessed data over 70 channels and 1,000 time points (data from elsewhere16). Insets show an expanded section with multiple overlapping spikes. b, Example simple templates centered at a single position on the probe (repeated at 1,536 positions for a probe), and example learned templates centered at different positions on the probe. c. Reconstruction of the data in panel "a" based on the templates in panel "b" and spike times. d, Residual after subtracting the reconstruction from the data. From Pachitariu, Sridhar, Pennington, Stringer, 2023
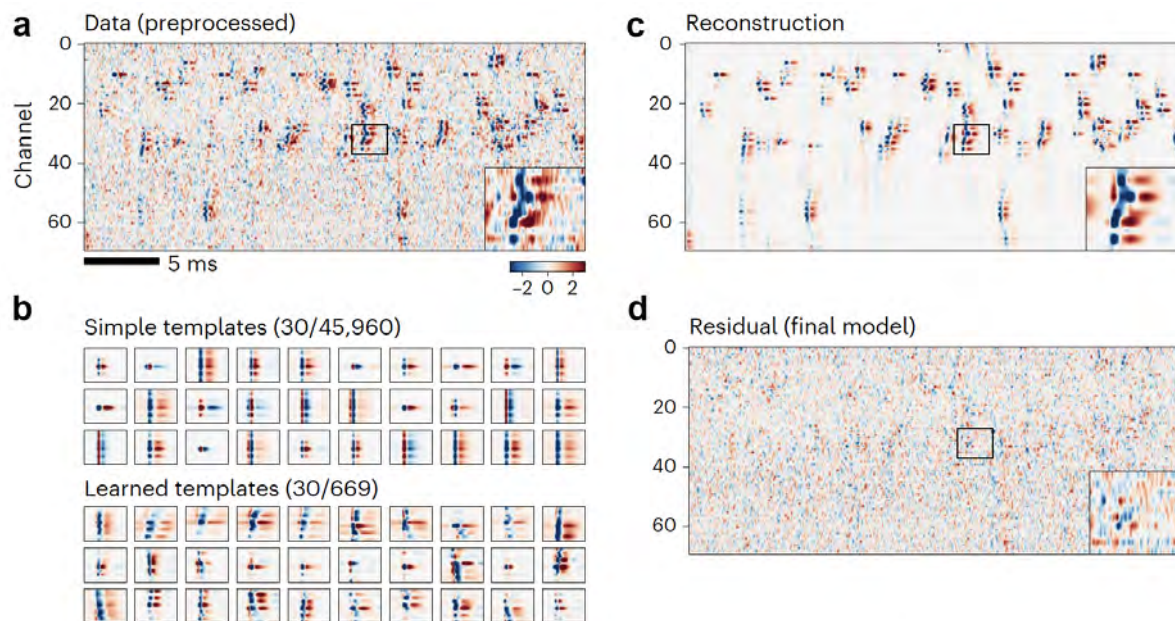
Figure 9: A unified open-source platform for unencumbered freely moving recordings. The top shows a simplified block diagram, illustrated via the tetrode headstage; multiple devices all communicate with the host PC over a single micro-coax cable via a serialization protocol. The bottom left shows the integrated nine-axis absolute orientation sensor and 3D tracking measure animal rotation, which drives the motorized commutator without the need to measure tether torque. The bottom center illustrates how mice were freely exploring a 3D arena made from Styrofoam pieces of varying heights. The bottom right showed the worst-case closed-loop latency, from neural voltage reading, to host PC, and back to the headstage. From Newman, Zhang, Cuevas-Lopez, Miller, Honda, van der Goes, Leighton, Carvalho, Lopes, Lakunina, Siegle, Harnett, Wilson, Voigts, 2025
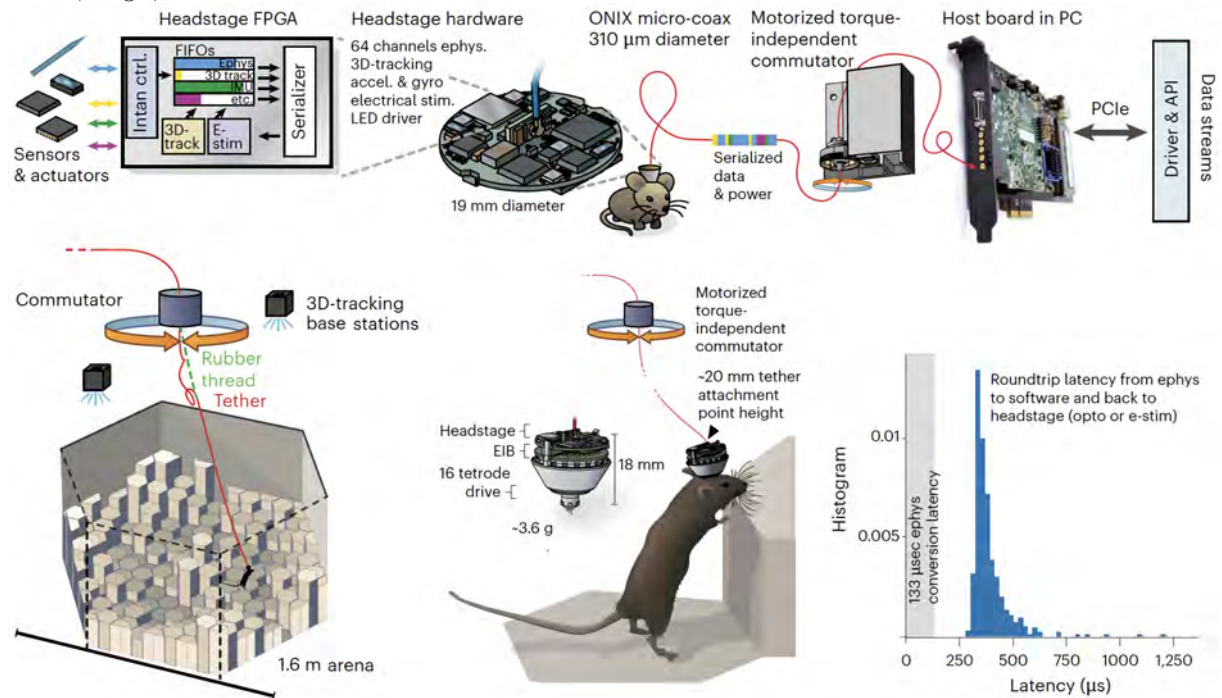
Figure 10: Stable long-term recordings during naturalistic locomotion. The top shows the position of one 3D-tracking sensor on the headstage during a seven hour long session in which the mouse was free to explore the 3D arena. Red trace and excerpt show an instance of the mouse spontaneously jumping from a lower to a higher tile. The bottom shows the 3D position, heading and smoothed firing rate of entire recording. From Newman, Zhang, Cuevas-Lopez, Miller, Honda, van der Goes, Leighton, Carvalho, Lopes, Lakunina, Siegle, Harnett, Wilson, Voigts, 2025

14
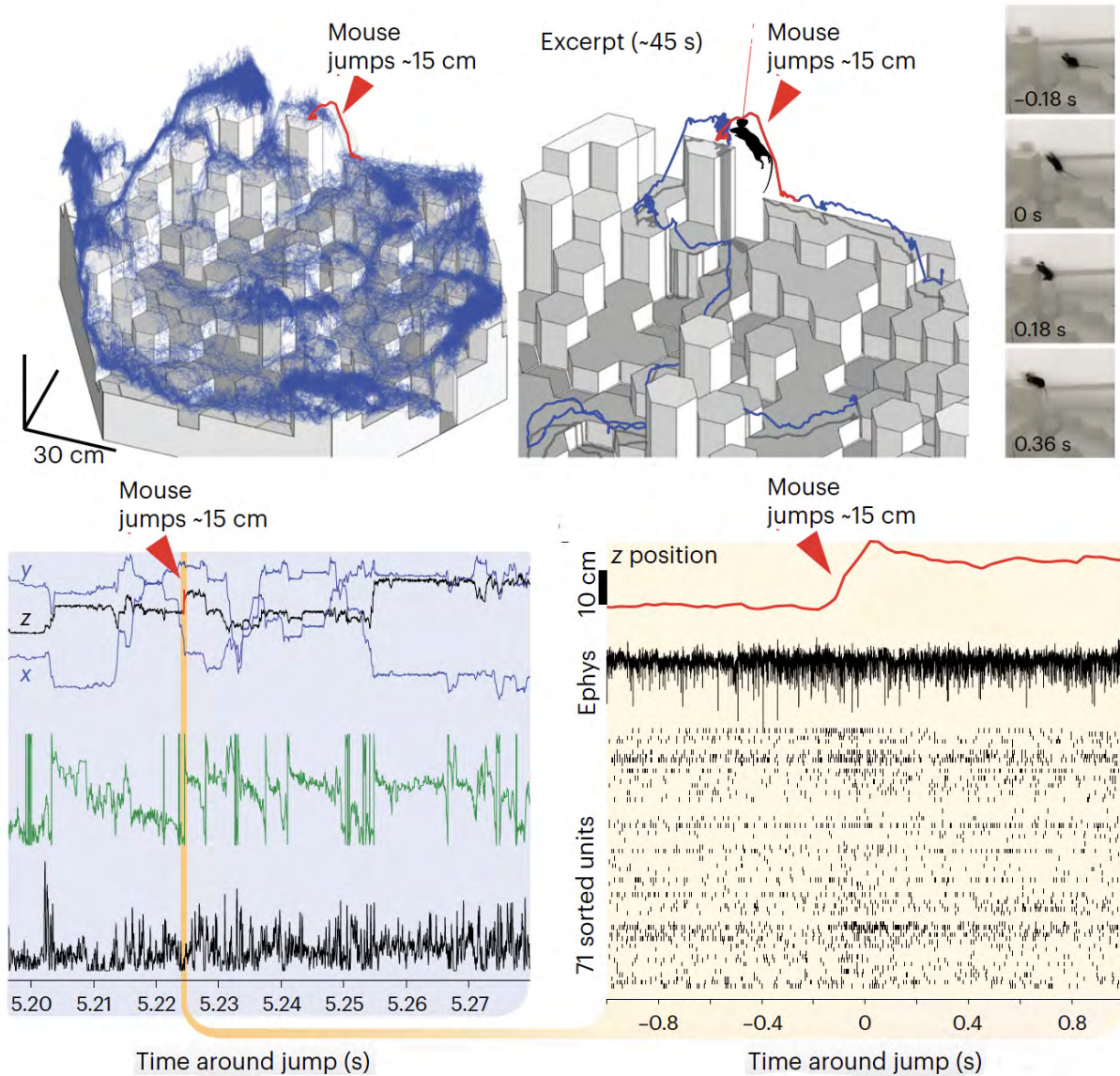
Figure 11: The cyclically permutable GFP turned into a detector of intracellular Ca^{2+}. From Chen, Wardill, Sun, Pulver, Renninger, Baohan, Schreiter, Kerr, Orger, Jayaraman, Looger, Svoboda and Kim, 2013.
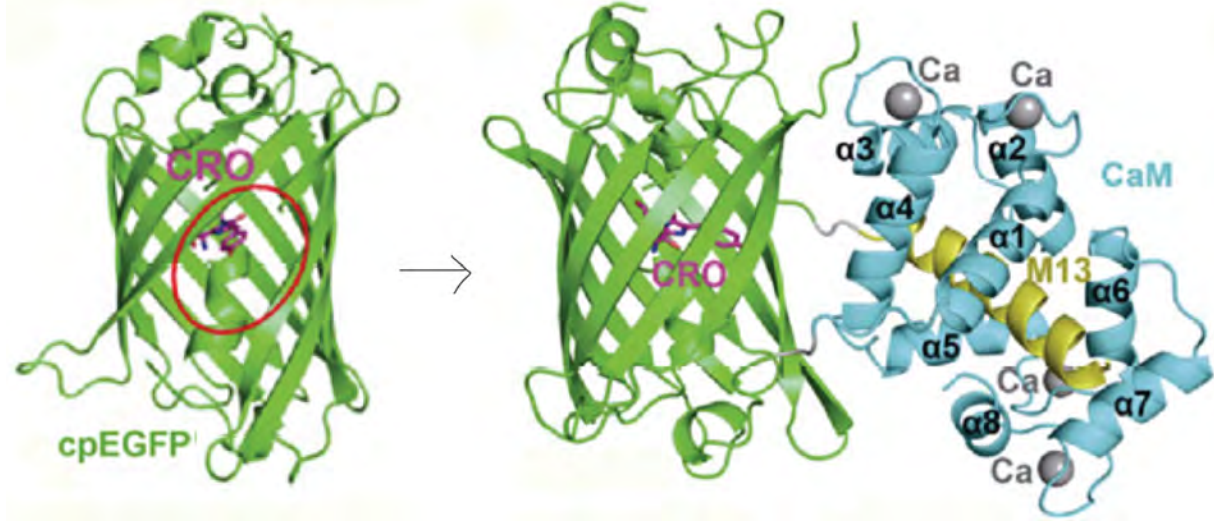
Figure 12: Absorption and fluorescent spectrum.
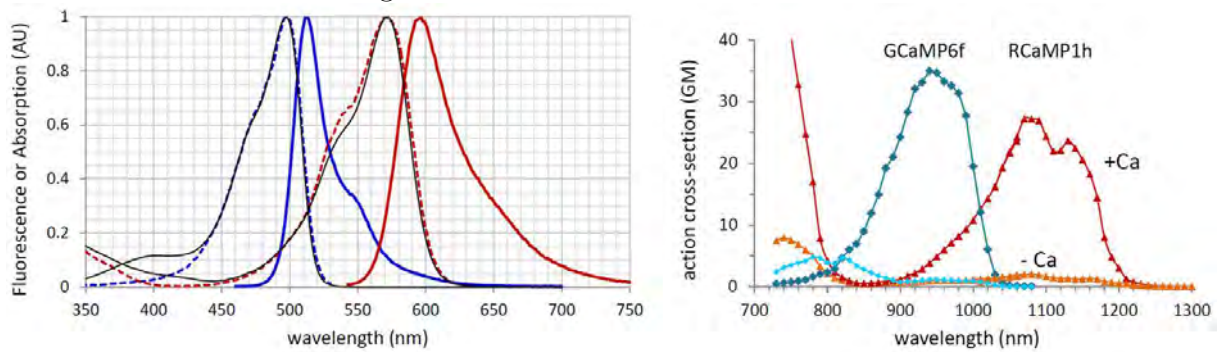
Figure 13: Intracellular Ca^{2+} recorded from mouse V1 with GCaMP8s. From Zhang, Rozsa, Liang, Bushey,Wei, Zheng, Reep, Broussard, Tsang, Tsegaye, Narayan, Obara, Lim, Patel, Zhang, Ahrens, Turner, Wang, , Korff, Schreiter, Svoboda, Hasseman, Kolb, Looger, 2023
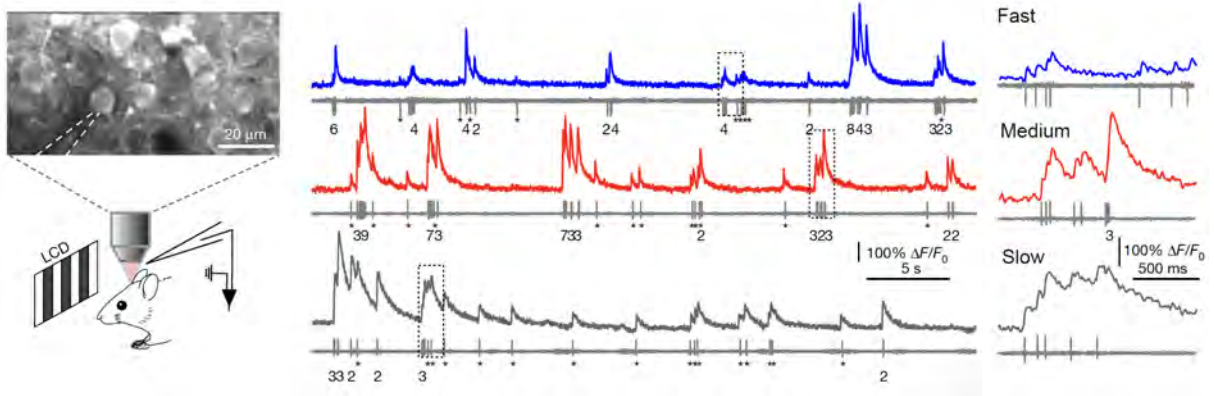
Figure 14: Essential components of a state-of-the-art two photon microscope. From Liu, Li, Marvin and Kleinfeld 2019.
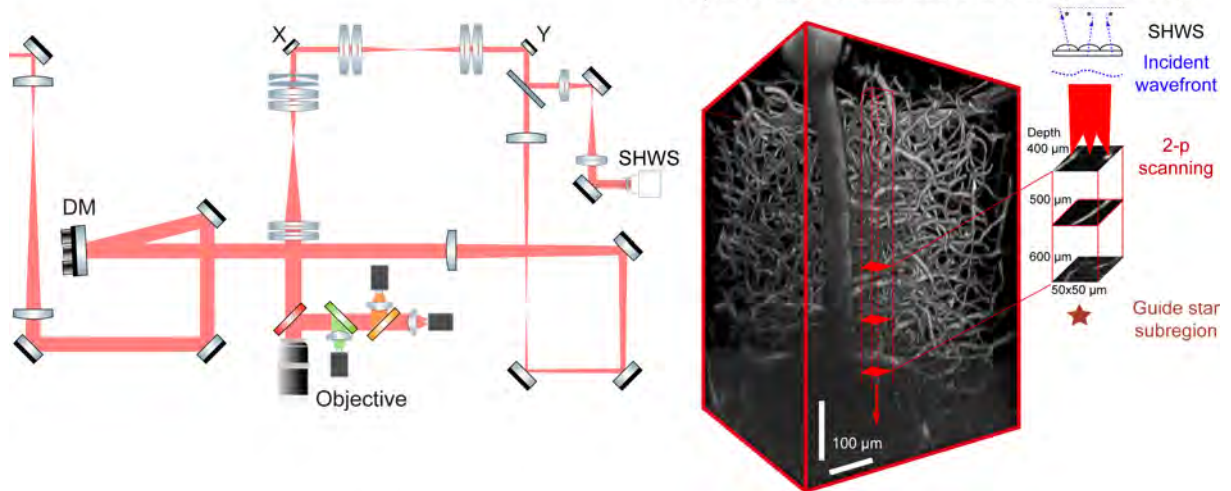
Figure 15: In vivo recording with adaptive optics from L5b in cortex of awake mice. From Liu, Li, Marvin and Kleinfeld 2019.
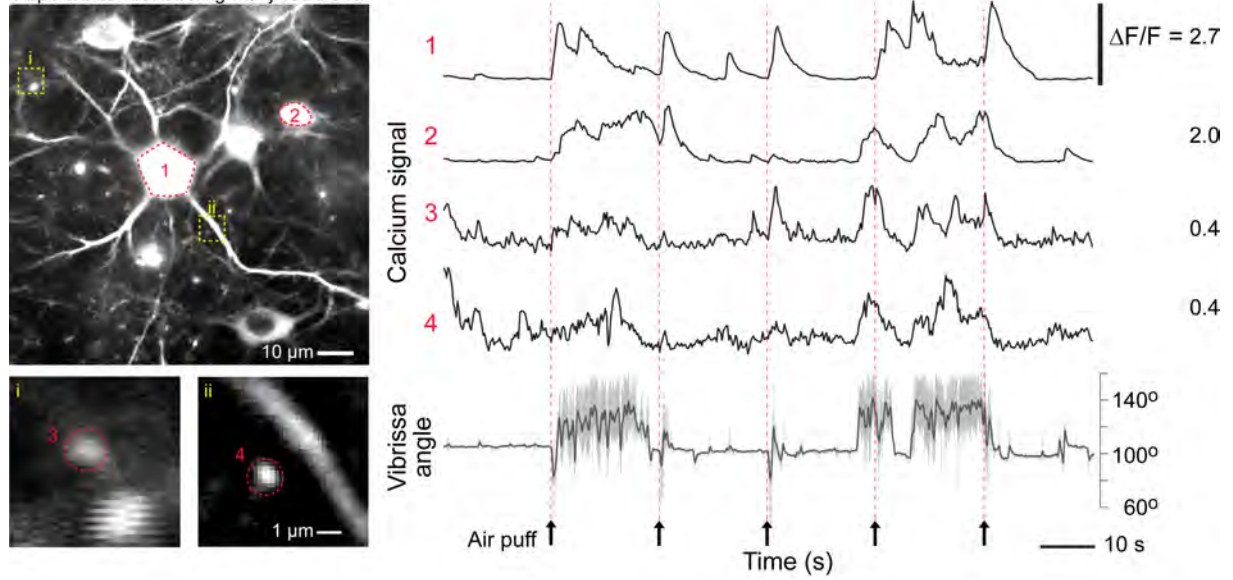
Figure 16: The distortion of cell images by the point spread function is most severe along the optical axis. From Tsai, Mateo, Field, Schaffer, Anderson and Kleinfeld, 2015.
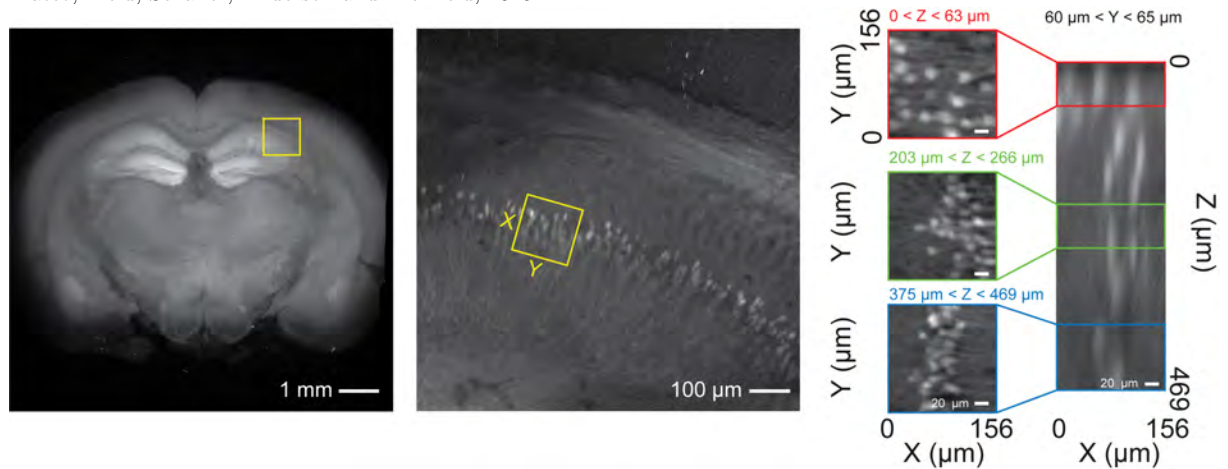
Figure 17: Intracellular responses in superficial V1 of mouse visual cortex using GCaMP6. From Chen, Wardill, Sun, Pulver, Renninger, Baohan, Schreiter, Kerr, Orger, Jayaraman, Looger, Svoboda and Kim, 2019.
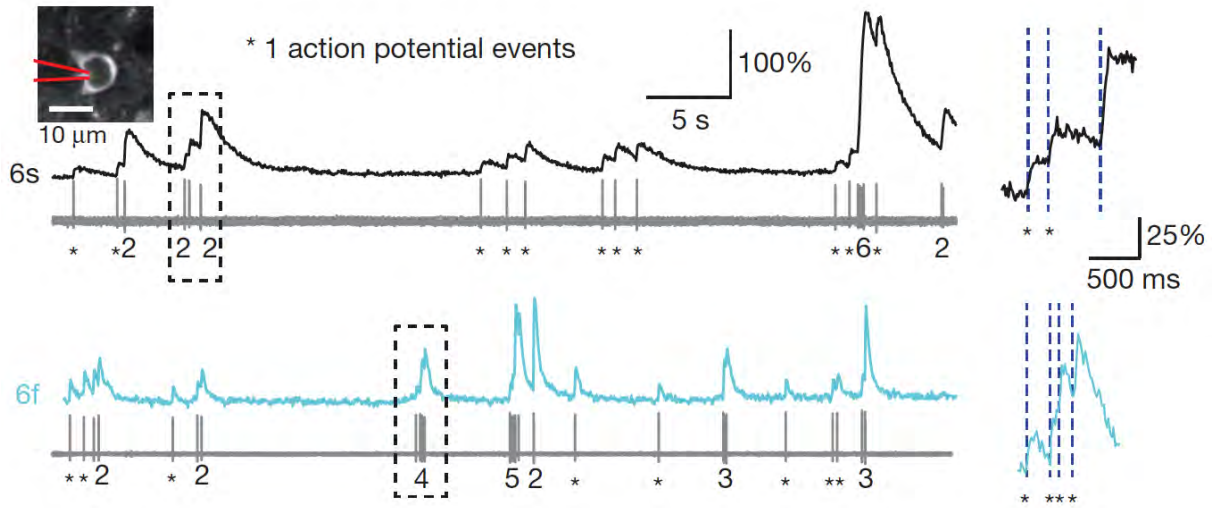
Figure 18: Intracellular responses in hippocampal brain slice with cell culture using Oregon Green BABTA. From Sasaki, Takahashi, Matsuki and Ikegaya, 2008.
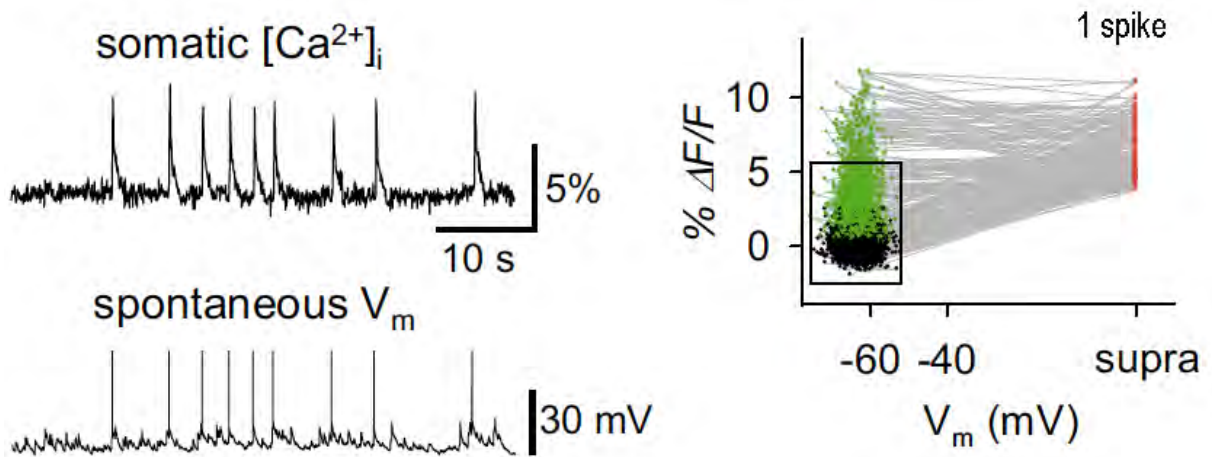
Figure 19: Intracellular Ca^{2+} can be an unreliable measure of spike count and may fail to detect single spikes in vivo. From Theis, Berens, Froudarakis, Reimer, Roson, Baden, Euler, Tolias and Bethge 2016.
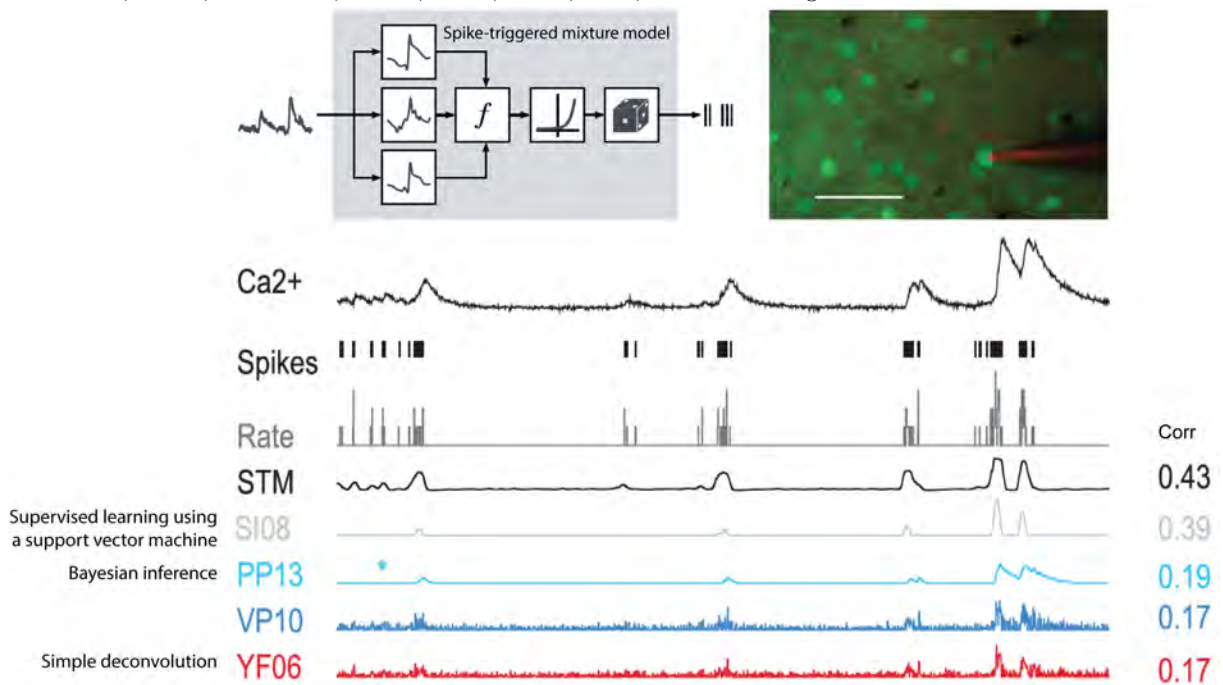
Figure 20: Intracellular Ca^{2+} in distal dendrites of L5b neurons can dissociate from somatic electrical activity. From Helmchen and Waters 2002.
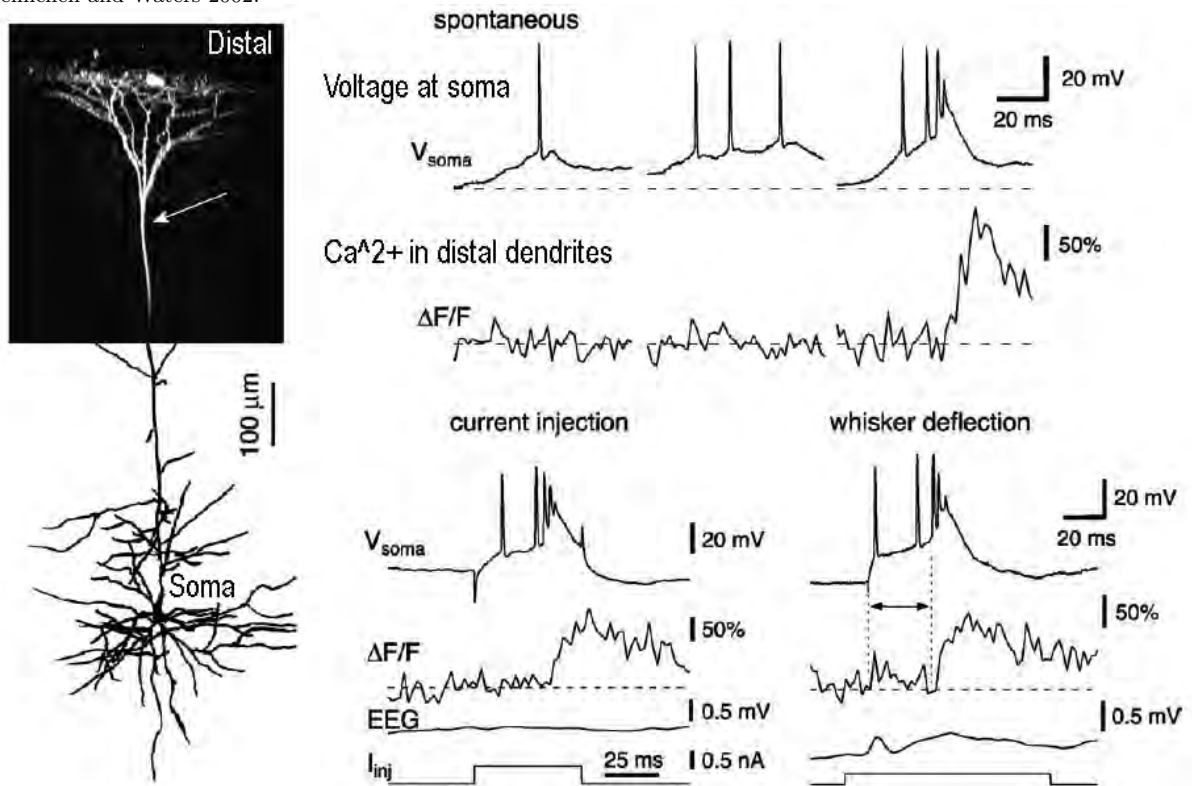
Figure 21: In vivo head-mounted 2P-scope. From Zong, Obenhaus, SkytÃ¸en, Eneqvist, de Jong, Vale, Jorge, Moser and Moser, 2022
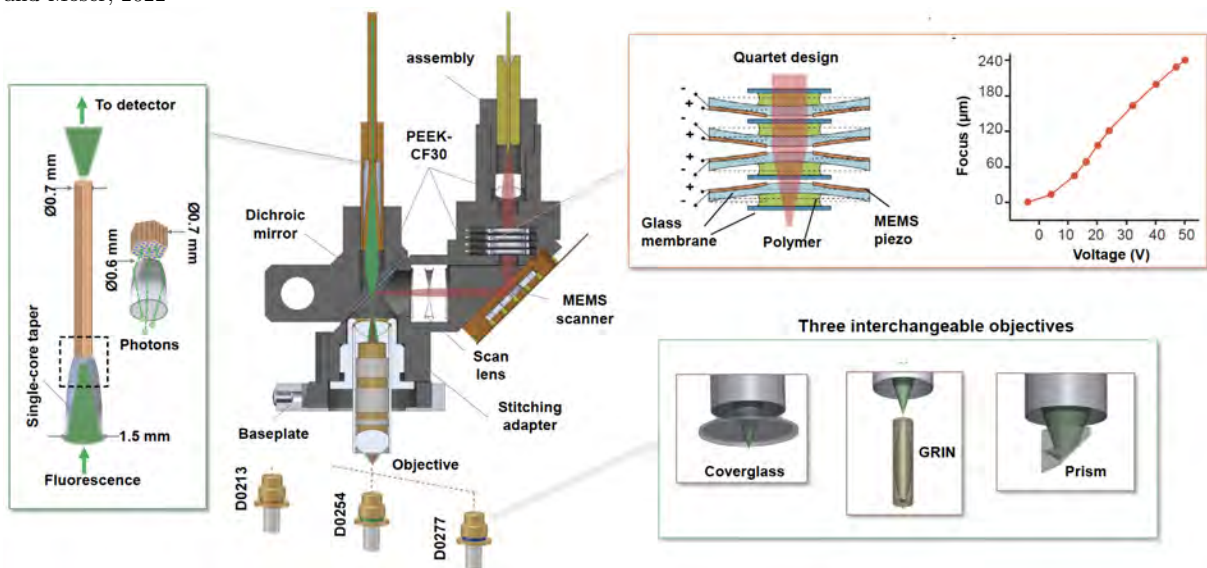
Figure 22: In vivo recording of grid cells im MEC with a head-mounted 2P-scope. From Zong, Obenhaus, SkytÃ¸en, Eneqvist, de Jong, Vale, Jorge, Moser and Moser, 2022
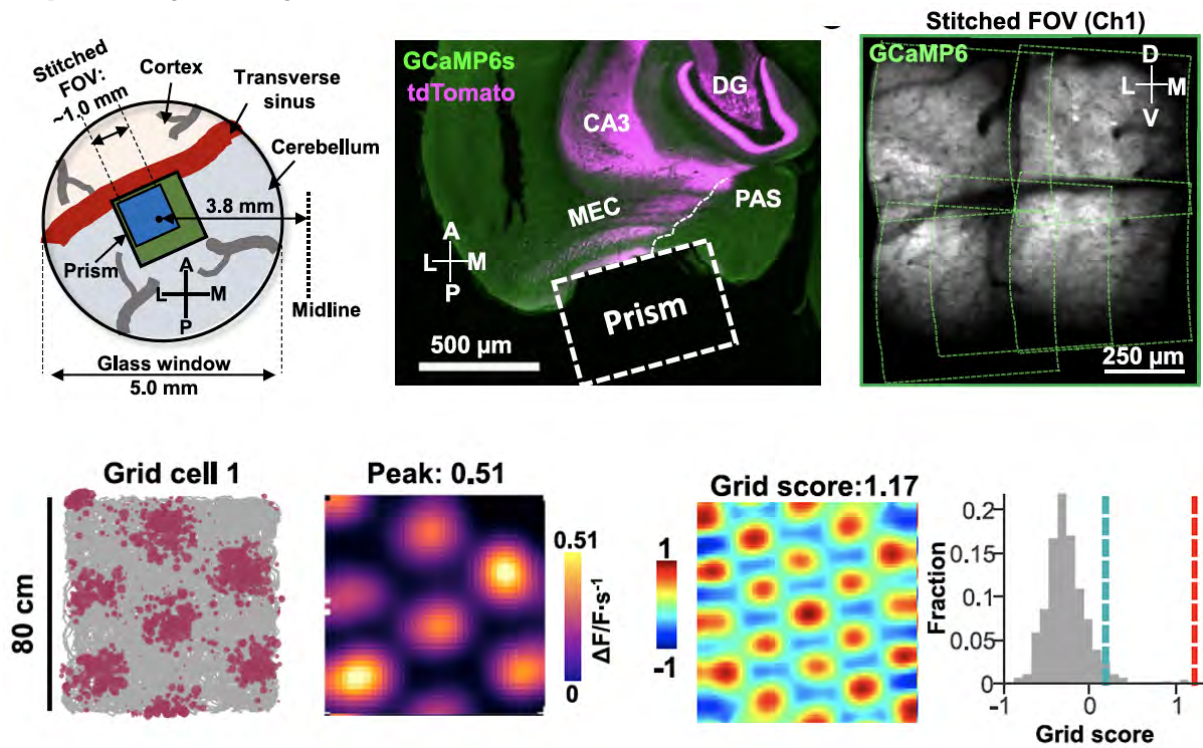
Figure 23: Fundamentals of light-sheet microscopy. 1. From Greger, Swoger and Stelzera, 2007
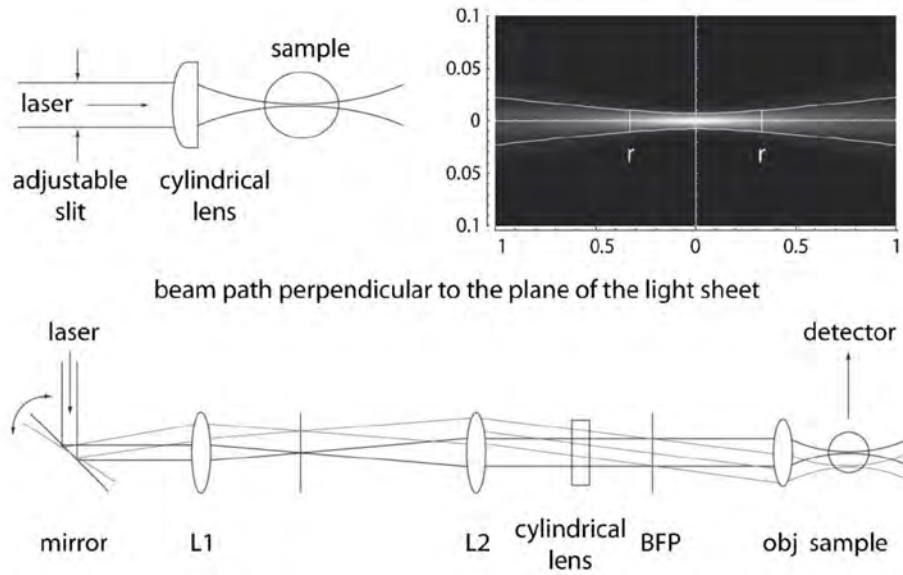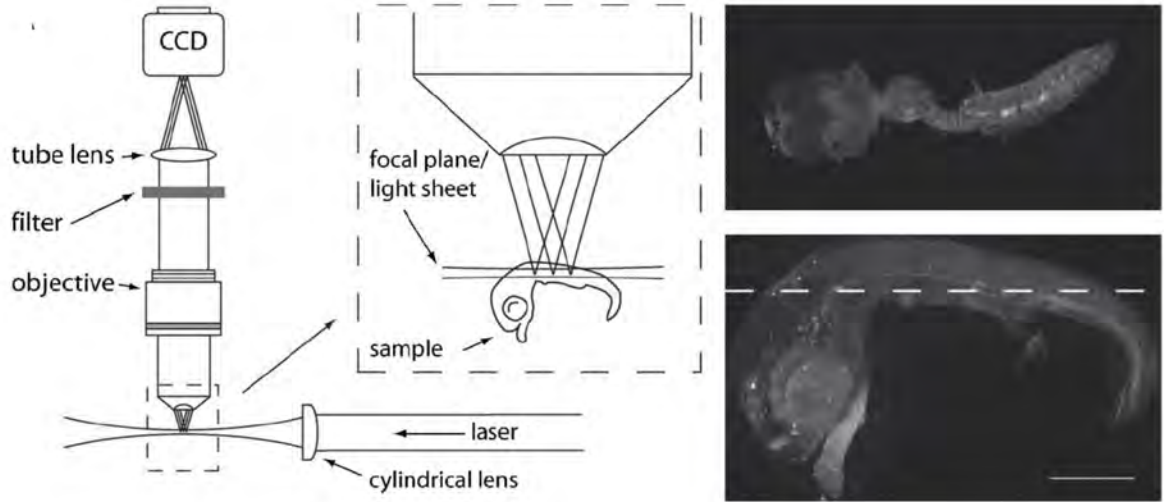
Figure 24: Fundamentals of light-sheet microscopy. 2. From Greger, Swoger and Stelzera, 2007
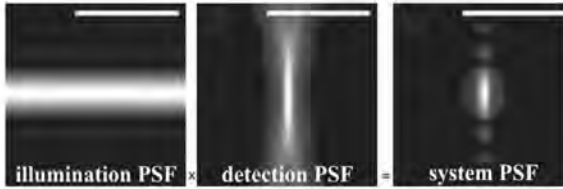
SPIM with a $10\times/0.3$ W detection objective lens. The length of the scale bar is 20 μm. The parameters are camera pixel pitch 4.65 μm, λ_{ill} =0.488 μm, λ_{det}=0.565 μm, n=1.33, image size 75 $\times$76 pixels, NA_{ill}=0.042, M_{det}=10, NA_{det}=0.3.

Lens	Technique	FWHM$_{lat}$ μm	FWHM$_{ax}$ μm	Volume al
$1.0\times/0.3$ W	FM	1.00	15.17	7943.0
	CFM	0.68	10.38	2513.1
	2hν-FM	1.22	18.57	14472.0
	SPIM	1.00	5.73	3000.2
$40\times/0.8$ W	FM	0.37	1.94	139.1
	CFM	0.25	1.33	43.5
	2hν-FM	0.45	2.38	252.3
	SPIM	0.37	1.65	118.3
$100\times/1.0$ W	FM	0.29	1.15	50.6
	CFM	0.20	0.79	16.5
	2hν-FM	0.36	1.40	95.0
	SPIM	0.29	0.99	43.6
$100\times/1.2$ W	FM	0.24	0.69	20.8
	CFM	0.16	0.47	6.3
	2hν-FM	0.29	0.84	37.0
	SPIM	0.24	0.65	19.6

The parameters are λ_{ill}=0.488 μm; NA_{ill}=0.034, 0.068, 0.108, and 0.108 for the $10\times/0.3$ W, $40\times/0.8$ W, $100\times/1.0$ W, and $100\times/1.2$ W lenses in the SPIM; camera pixel pitch 6.45 μm; number of pixels=1024$\times$1344; λ_{det}=0.520 μm; n=1.33; λ_{ill} =0.900 μm for two-photon excitation.

Figure 25: Application of light-sheet microscopy to recording calcium signals from zebra fish. From Ahrens, Orger, Robson, Li and Keller, Meth 2013
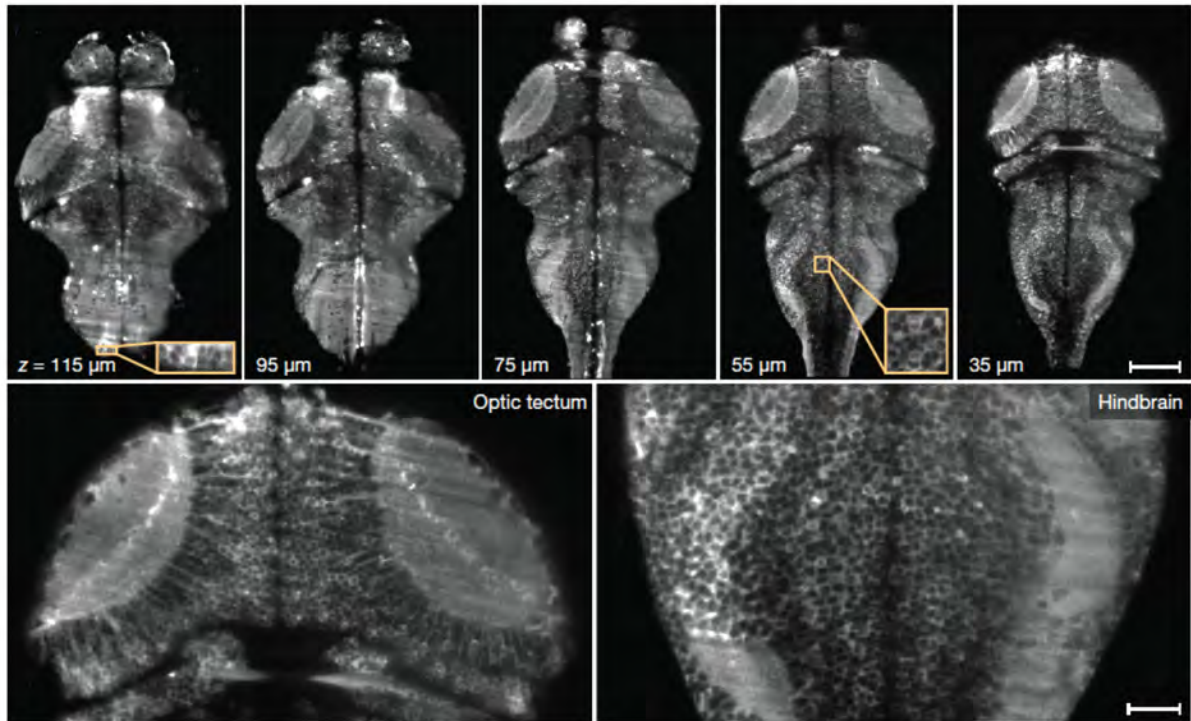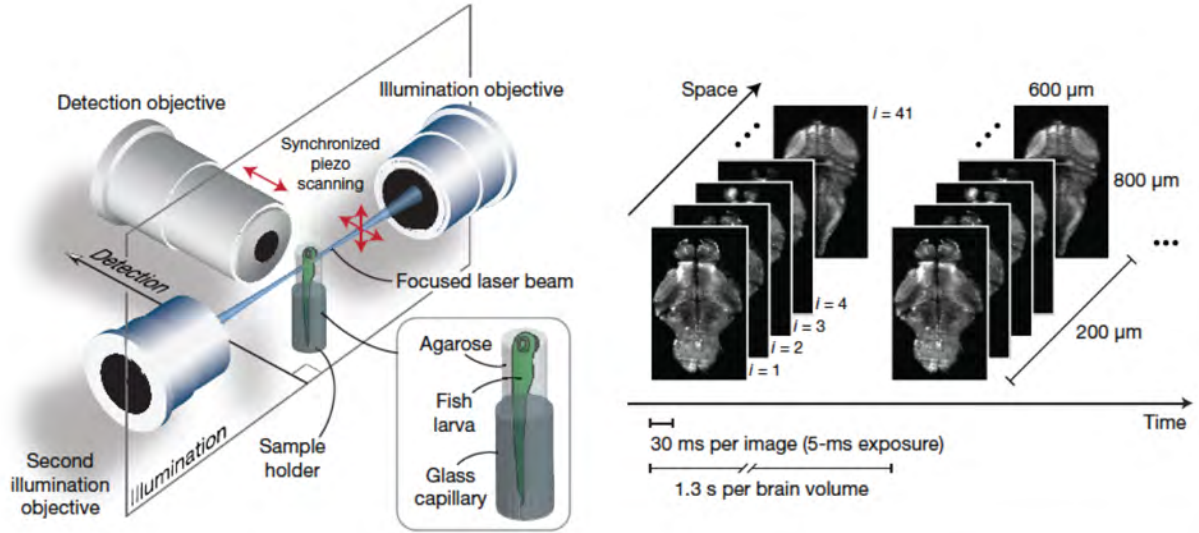
Figure 26: In vivo hippocampus preparation. From Dombeck, Harvey, Tian, Looger and Tank 2010.
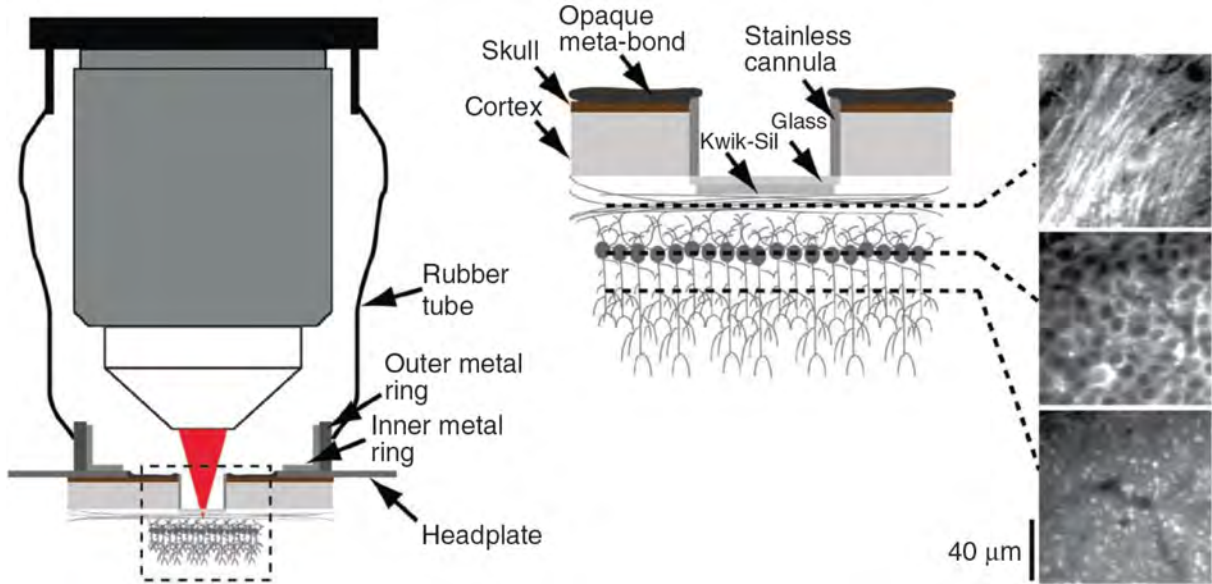

Figure 27: In vivo recording in hippocampus. From Dombeck, Harvey, Tian, Looger and Tank 2010.
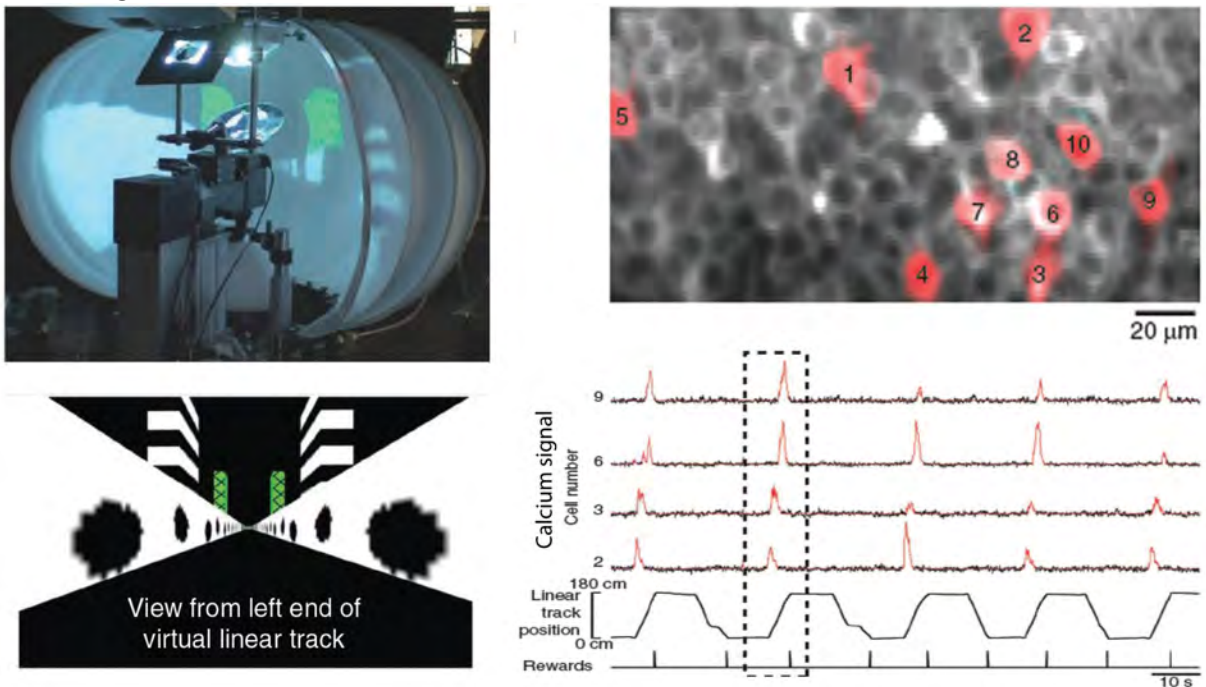
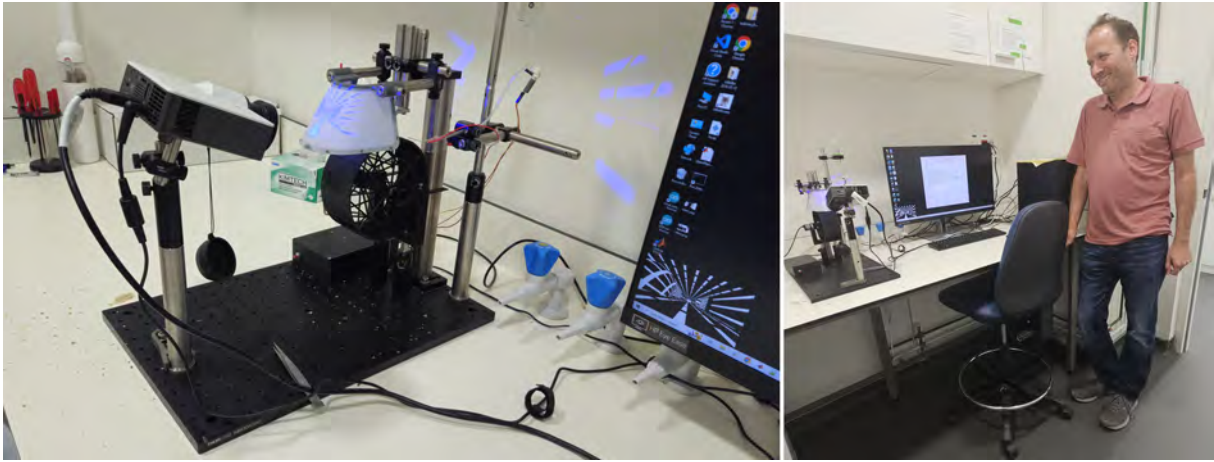Figure 28: In vivo hippocampus preparation recorded in a minimal virtual set-up with 1P voltage imaging. From Yael Cohen, as used in Cohen et al 2019.

Figure 29: Natural transmembrane proteins that use light to pump ion of open ion selective pores.
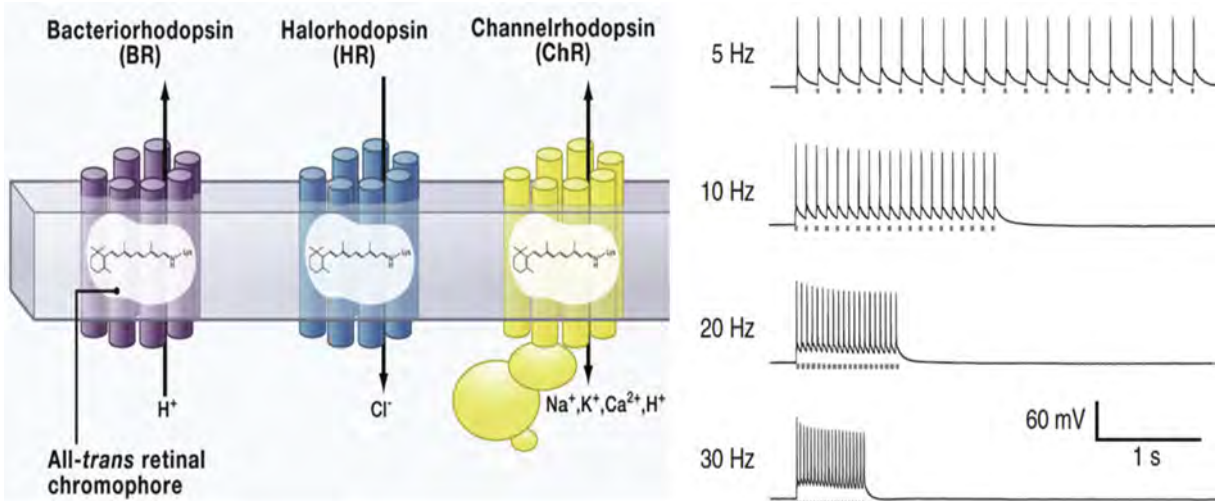
Figure 30: One photon absorption and dynamics of channelrhodopsin. From Klapoetke, Murata, Kim, Pulver, Birdsey-Benson, Cho, Morimoto, Chuong, Carpenter, Tian, Wang, Xie, Yan, Zhang, Chow, Surek, Melkonian, Jayaraman, Constantine-Paton, Wong and Boyden, 2014
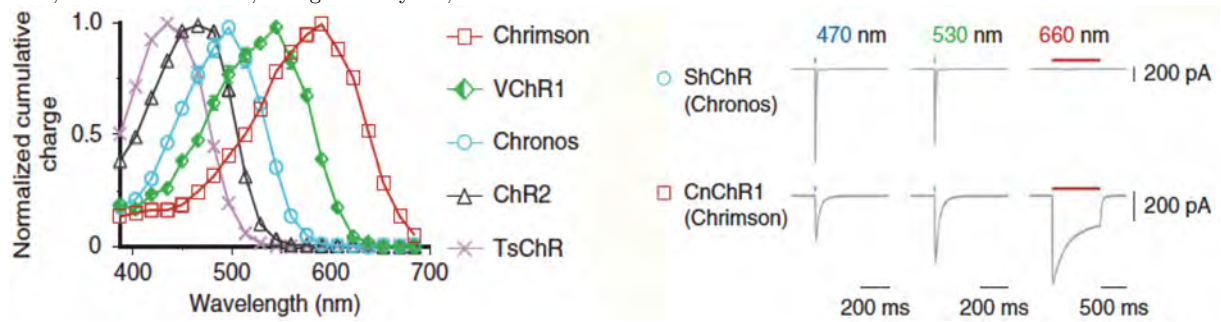

Figure 31: Two-photon action spectra for activating neurons with red-shifted channelrhodopsin C1V1 and action spectrum for recording Ca^{2+} transients with GCaMP3.
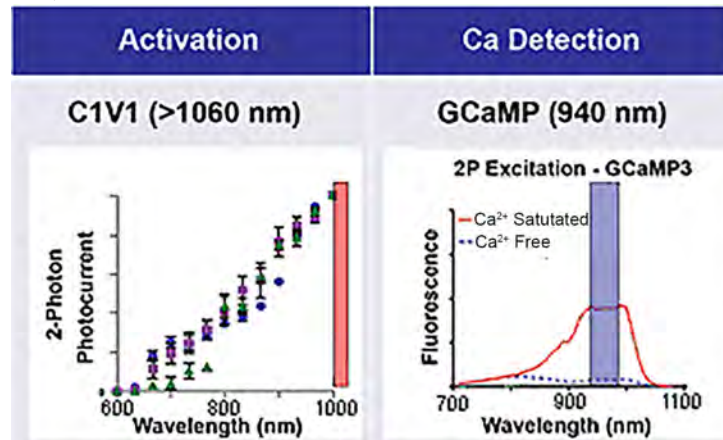
Figure 32: Narrow range of excitation for two-photon activation with red-shifted channelrhodopsin ReaChR. From Chaigneau, Conzitti, Gajowa, Soler-Llavina, Tanese, Brureau, Papagiakoumou, Zeng and Emiliani, 2016
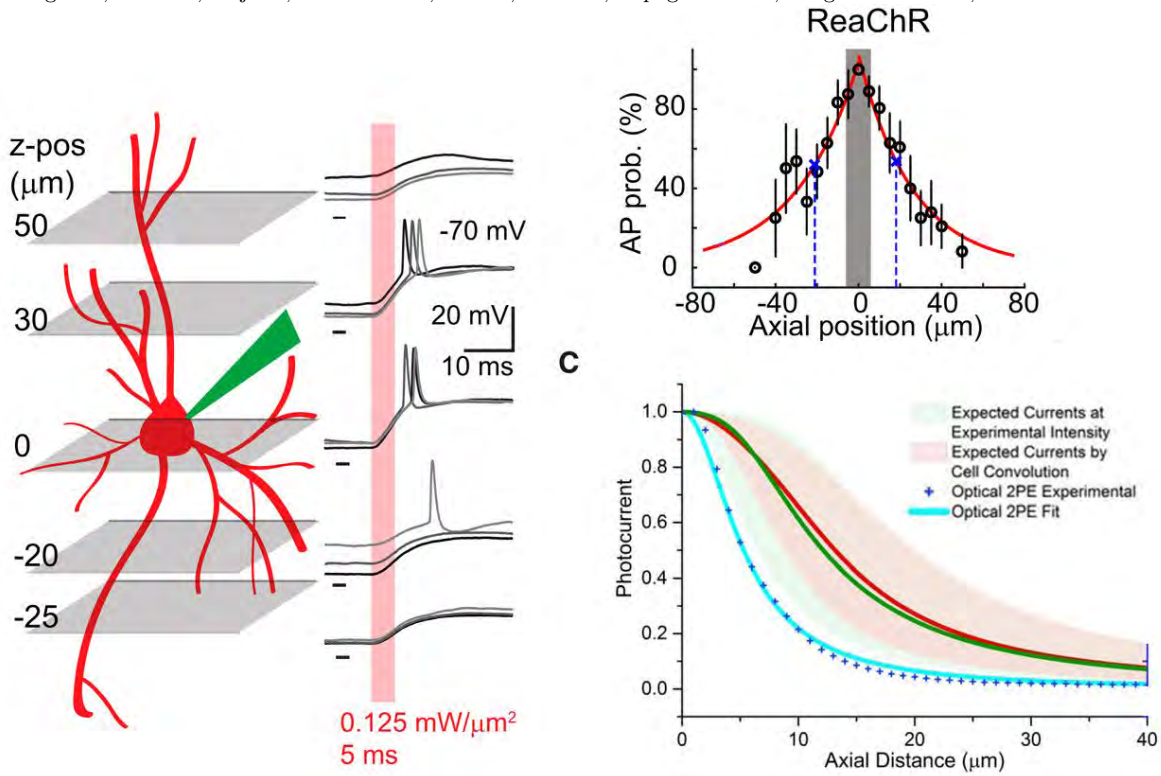

Figure 33: Schematic for feedback induced long-term synaptic potentiation. From Zhang, Russell, Packer, Gauld and Hausser 2018.
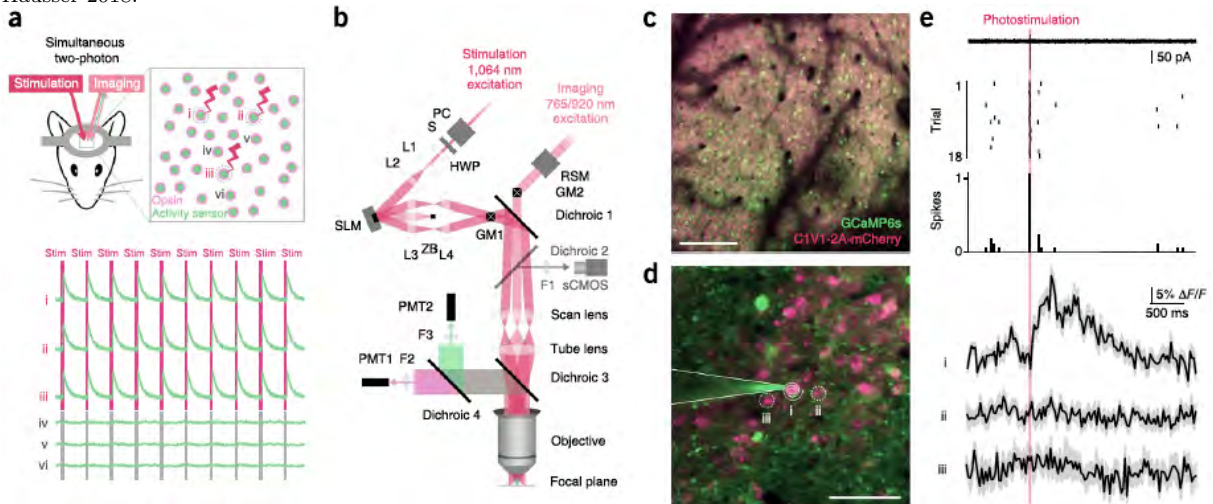
Figure 34: Test of feedback induced long-term synaptic potentiation. From Zhang, Russell, Packer, Gauld and Hausser 2018.
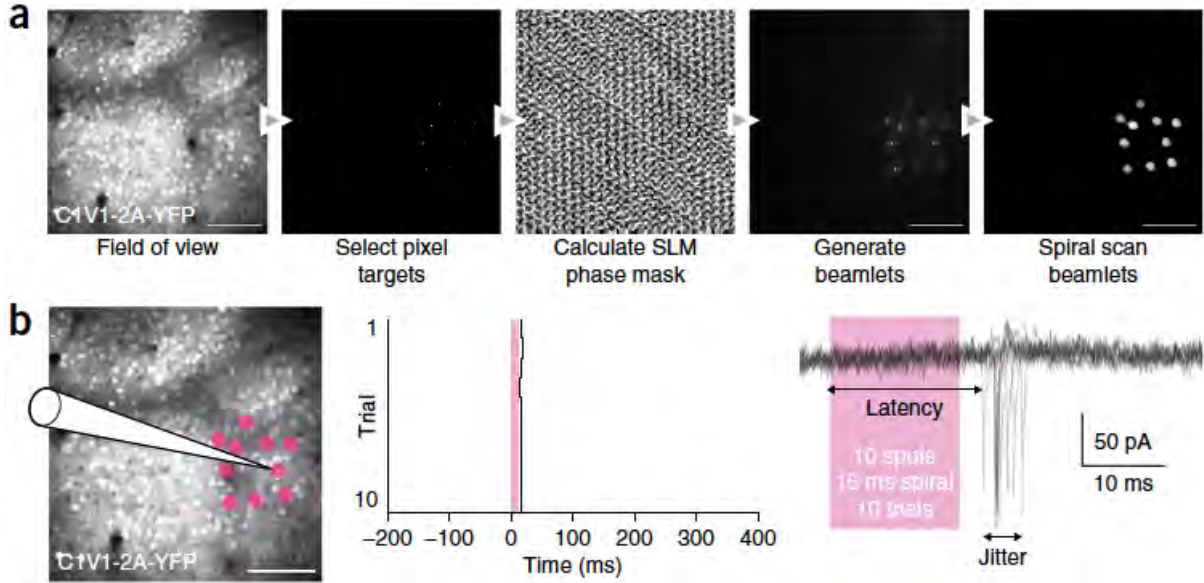

Figure 35: Test of feedback induced long-term synaptic potentiation. From Zhang, Russell, Packer, Gauld and Hausser 2018.